

# Unbinding Pathways of GW4064 from Human Farnesoid X Receptor As Revealed by Molecular Dynamics Simulations

Weihua Li,<sup>†,‡</sup> Jing Fu,<sup>†</sup> Feixiong Cheng,<sup>†</sup> Mingyue Zheng,<sup>\*,‡</sup> Jian Zhang,<sup>§</sup> Guixia Liu,<sup>†</sup> and Yun Tang<sup>\*,†</sup>

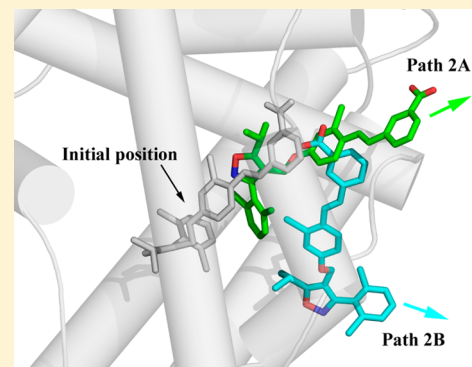
<sup>†</sup>Shanghai Key Laboratory of New Drug Design, School of Pharmacy, East China University of Science and Technology, Shanghai 200237, China

<sup>‡</sup>State Key Laboratory of Drug Research, Shanghai Institute of Materia Medica, Chinese Academy of Sciences, Shanghai 201203, China

<sup>§</sup>Shanghai Key Laboratory of Tumor Microenvironment and Inflammation, School of Medicine, Shanghai Jiao Tong University, Shanghai 200025, China

## Supporting Information

**ABSTRACT:** Farnesoid X receptor (FXR, NR1H4) is a member of a nuclear receptor superfamily, which plays important roles in bile acid homeostasis, lipoprotein and glucose metabolism, and hepatic regeneration. GW4064 is a potent and selective FXR agonist and has become a tool compound to probe the physiological functions of FXR. Until now, the mechanism of GW4064 entering and leaving the FXR pocket is still poorly understood. Here, we report a computational study of GW4064 unbinding pathways from FXR by using several molecular dynamics (MD) simulation techniques. Based on the crystal structure of FXR in complex with GW4064, conventional MD was first used to refine the binding and check the stability of GW4064 in the FXR pocket. Random acceleration MD simulations were then performed to explore the possible unbinding pathways of GW4064 from FXR. Four main pathway clusters were found, among which three subpathways, namely Paths 2A, 2B, and 1B, were observed most frequently. Multiple steered MD simulations were further employed to estimate the maximum rupture force and the sum of the forces and to characterize the intermediate states of the ligand unbinding process. By comparing the average force profiles and structural changes, Paths 2A and 2B were identified to be the most favorable unbinding pathways. The former is located between the H1–H2 loop and the H5–H6 loop, and the latter is located in the cleft formed by the H5–H6 loop, H6, and H7. Moreover, the residues lining the pathways were analyzed for their roles in ligand unbinding. Based on our results, the possible structural modification strategies on GW4064 were also proposed.



## INTRODUCTION

Farnesoid X receptor (FXR, NR1H4) is a member of the nuclear receptor (NR) superfamily highly expressed in the liver, gall bladder, intestine, kidneys, and adrenal glands.<sup>1–4</sup> As a sensor for bile acids, FXR regulates many aspects of bile acid homeostasis, metabolism, and enterohepatic circulation. Besides its vital role in the bile acid homeostasis, FXR also regulates the expression of target genes involved in the triglyceride synthesis and metabolism.<sup>5</sup> Recently, several studies confirmed the importance of FXR on modulating gluconeogenesis, glycogen synthesis, and insulin sensitivity.<sup>2,6</sup> Hence, FXR has been suggested to be a potential drug target in the treatment of metabolic diseases, such as dyslipidemia, atherosclerosis, gallstone disease, cholestasis, and diabetes.<sup>7,8</sup>

So far, many compounds with different scaffolds have been identified to exhibit potent activation effects on FXR, including GW4064, 6α-ethyl-chenodeoxycholic acid (6E-CDCA), fexaramine, XL335, and benzimidazole derivatives.<sup>9,10</sup> As a highly potent and selective nonsteroidal FXR agonist, GW4064 has become a tool compound used for investigating the physiological functions of FXR.<sup>11–14</sup> However, GW4064 is

not an ideal drug candidate due to some apparent limitations, such as UV light instability, potentially toxic stilbene pharmacophore, and poor pharmacokinetic properties.<sup>15,16</sup> Accordingly, considerable efforts have been devoted to structural modification of GW4064 with aim to improve its drugability.<sup>15–18</sup>

Recently, a new approach based on the ligand–receptor interactions along the unbinding pathway was proposed for structural optimization of a compound.<sup>19,20</sup> This method requires the knowledge of unbinding pathway *a priori*, which is not trivial for those proteins whose binding pocket is buried into the protein core with no obvious channels for ligand unbinding. Unfortunately, FXR is one of the typical examples of such proteins. For potentially employing this new method in structural modification of GW4064, there is a great interest in identifying the unbinding pathways of GW4064 from FXR ligand-binding domain (LBD).

Received: August 22, 2012

Published: October 28, 2012

The issue of ligand binding/unbinding pathways from NR LBDs has attracted much attention in the past decade. Structural comparison of NR LBDs in complex with agonists or antagonists and unliganded LBDs reveals that the ligand binding induces a significant repositioning of helix 12 (H12).<sup>21</sup> This led to the so-called mousetrap mechanism by which the ligand entry or exit is regulated by H12.<sup>22</sup> Computational methods based on molecular dynamics simulations (MD) have been extensively used for identifying the possible ligand binding/unbinding pathways in several NRs. Steered MD (SMD), locally enhanced sampling (LES) MD, and random acceleration MD (RAMD) simulations were used to explore the possible ligand binding/unbinding pathways in retinoic acid receptor (RAR, NR1B3).<sup>23–25</sup> Two most likely pathways were identified for the ligand entry/exit in RAR. One pathway is close to H12 which is similar to the mousetrap mechanism, and the other is between the H1–H3 loop and H3. Skaf and co-workers applied LES MD simulations to investigate the possible ligand dissociation pathways from thyroid hormone receptors (TRs, NR1A).<sup>26</sup> Three distinct pathways were discovered that can be used for the ligand dissociation. In a subsequent study,<sup>27</sup> the same group used SMD simulations to identify the most likely ligand escape pathway, which is located between the H1–H3 loop and H3. LES MD, SMD, and RAMD simulations have also been applied to study the possible ligand escape routes from estrogen receptors (ERs, NR3A).<sup>28–30</sup> The results showed that ligands could dissociate from ERs through multiple pathways. Both the H11–H12 loop and H1–H3 loop regions could serve as the ligand dissociation routes depending on the character of ligands. Targeted MD (TMD) simulations were also employed to probe the ligand unbinding pathways from the vitamin D receptor (VDR, NR1I1)<sup>31</sup> and the peroxisome proliferator-activated receptor gamma (PPAR $\gamma$ , NR1C3).<sup>32</sup> These findings have suggested that different NRs may have different pathways for ligand binding/unbinding, and the preference of pathways is dependent on the character of ligands.

In the present work, we aim to reveal the unbinding pathway and the associated unbinding mechanism of GW4064 from FXR. To this end, 30-ns conventional MD simulations were first performed on the systems of FXR in complex with GW4064. After that, based on the snapshots from the equilibrated system, multiple RAMD simulations were employed to explore the possible ligand unbinding routes. By analyzing the successful unbinding trajectories and using SMD simulations, the most likely unbinding pathway was determined, and the associated unbinding mechanism was finally elucidated.

## MATERIALS AND METHODS

**System Preparation.** The starting structure of human FXR in complex with GW4064 and a coactivator peptide (FXR/GW4064/AF2)<sup>16</sup> for MD simulations was taken from Protein Data Bank (PDB, entry code: 3DCT at 2.5 Å resolution). To investigate the effects of the coactivator on the unbinding pathways, another system that only contains FXR and GW4064 (FXR/GW4064) was constructed by removing the coordinates of the bound peptide from 3DCT. The protonation states of the ionizable residues and histidines were determined by PROPKA.<sup>33</sup> Based on the calculated pK<sub>a</sub> values and the microenvironment, His254, His313, His422, His429, and His446 were assigned to be fully protonated at both nitrogen

atoms. His294 was protonated at  $\delta$  nitrogen and other histidine residues at  $\epsilon$  nitrogen atoms.

The initial model of GW4064 was extracted from 3DCT. Geometric optimization of GW4064 was conducted at the B3LYP/6-31G\*\* level using Gaussian03 [www.gaussian.com]. Atomic charges of GW4064 were derived from the optimized structure by using restrained electrostatic potential (RESP) fitting procedure.<sup>34</sup> The Leap program of AMBER9<sup>35</sup> was used to produce force field, topology, and coordinate files of the FXR complexes. All crystallization water molecules were kept in the initial models. The resulted models were solvated with TIP3P<sup>36</sup> water in a cubic periodic box. Counterions were added to neutralize the systems. The distance between the box walls and the closest protein atom was set to 10.0 Å.

**Conventional MD Simulations.** Conventional MD simulations were performed using the AMBER9 program.<sup>35</sup> The AMBER 99SB all atom force field was used for the proteins, and the general AMBER force field was used for the agonist. The detailed procedure for MD simulation was adopted as previously described.<sup>37,38</sup> Briefly, energy minimization was carried out with decreasing the harmonic force restraints to protein atoms. The minimized systems were then gradually heated from 0 to 300 K over 60 ps under the NVT ensemble condition and equilibrated at 300 K for 100 ps. Finally, a 30-ns MD simulation was conducted under the NPT ensemble at 300 K and 1 atm. The SHAKE algorithm<sup>39</sup> was applied to constrain the covalent bonds to hydrogen atoms. The Particle Mesh Ewald method<sup>40</sup> was adopted to calculate the long-range electrostatic interactions. The time step of 2 fs and nonbonding interaction cutoff radius of 10 Å were used. The simulation trajectories were saved every 1.0 ps.

**Random Acceleration Molecular Dynamics (RAMD) Simulations.** RAMD<sup>41,42</sup> is an enhanced sampling approach that makes a ligand release from the buried protein active site within a relatively short time scale (from picoseconds to nanoseconds). In RAMD, a randomly oriented force is applied to the center of mass of the ligand with aim to accelerate the ligand expulsion from the active site to the protein surface. Within a preset number of MD steps ( $N$ ), the direction of the random force is maintained. After  $N$  steps of MD simulation, the distance that the ligand moves is calculated. If the ligand reaches the predefined threshold distance ( $r_{\min}$ ), the same direction is kept for another  $N$  steps; otherwise, a new force direction is chosen randomly. The advantage of RAMD is that the ligand can automatically search for the dissociation pathways without predefining the direction, which is required in the SMD method.

In any RAMD application, the size and effect of the artificial force exerted on the ligand should be kept as low as possible. After initial trials of effect of different magnitudes of accelerations on the ligand exit, two magnitude accelerations, 0.25 and 0.20 kcal•Å<sup>-1</sup>•g<sup>-1</sup>, were used in this study. These acceleration magnitudes have been adopted in several previous studies. The  $N$  was set to 40 and 80 steps, respectively. The threshold distance  $r_{\min}$  was set to 0.001, 0.005, and 0.01 Å, separately. A simulation is terminated either when the ligand has moved 30 Å from its original position or the simulation time has reached 4 ns. 100 RAMD simulations were run for each system by combining different RAMD parameters (Supporting Information Table S1) and random seeds, which resulted in a total of 200 RAMD simulations trajectories for the two systems.

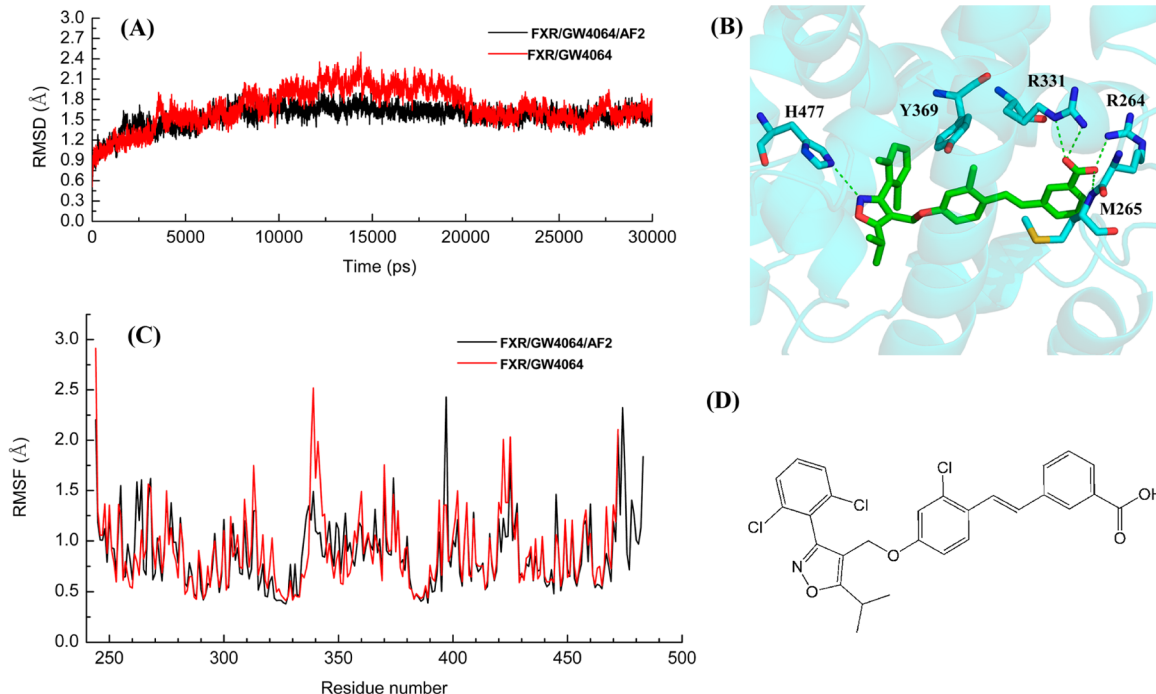


**Figure 1.** (A) RMSD variation of backbone atoms in FXR/GW4064/AF2 (black) and FXR/GW4064 (red) with respect to simulation time. (B) A close view of GW4064 bound in the FXR pocket after MD simulation. Important residues are labeled. (C) RMSF of backbone atoms versus residue position of FXR/GW4064/AF2 (black) and FXR/GW4064 (red). (D) The two-dimensional structure of GW4064.

**Steered Molecular Dynamics (SMD) Simulations.** SMD<sup>43,44</sup> applies an external force to the center of mass of the ligand to pull it out from the protein active site along a predefined direction. The SMD pulling directions in the FXR complexes were determined by the statistical results of RAMD simulations. The pulling directions were set by defining two atom groups, the initial location of the ligand in the FXR active site and the C $\alpha$  atom of Tyr382 (Path 1B), Trp454 (Path 2A), and Leu748 (Path 2B), respectively. The constant-velocity SMD simulations were performed in the present simulations. The pulling velocity was set to 0.01 Å•ps<sup>-1</sup>, which was slower than those used in other nuclear receptors by the same method.<sup>29–31</sup> A spring constant of 4 kcal•mol<sup>-1</sup>•Å<sup>-2</sup> was applied to the center of mass of the ligand. In order to prevent the translation and rotation of the protein, positional restraints of three C $\alpha$  atoms of Ile256 in helix 1, Leu319 in helix 4, and Leu433 in helix 10 were applied by using a harmonic potential with a force constant of 50 kcal•mol<sup>-1</sup>•Å<sup>-2</sup>.

The force exerted on the ligand is defined as

$$F(t) = 2k(vt - x(t)) \quad (1)$$

where  $k$  is the spring constant of the constraint;  $v$  is the pulling velocity; and  $x(t)$  is the position of the ligand at time  $t$ .

SMD simulations were carried out starting from the snapshot structure at 30 ns. Ten SMD simulations were repeatedly performed with different random seeds for computing the maximum force and the sum of the force.

## RESULTS AND DISCUSSION

### Structural Stability in Conventional MD Simulations.

The structural stability of FXR complexes in conventional MD simulations was examined by analyzing the root-mean-square deviation (RMSD) variations of protein backbone atoms and the ligand atoms relative to their initial structures. Figure 1A

shows the RMSD variations of the two systems with respect to simulation time. The RMSD values have a large fluctuation in the first 20-ns and reach stability thereafter. The protein atoms do not deviate from their initial structures, and the RMSD values of the two systems converge to 1.5 Å. Similarly, the RMSD values of the ligand in the two systems converge to 1.1 Å after the systems reach stability (Supporting Information Figure S1). The internal coordinates of GW4064 in the two systems were preserved. However, the isoxazole ring of GW4064 in both systems has about 1.1 Å shift toward His447 relative to their crystal structures. In the crystal structure, the distance between the His447 NE2 atom and the N atom of the GW4064 isoxazole ring is about 3.6 Å. The same distance was shortened to 3.1 Å after MD simulations, in which a direct hydrogen bond was formed between the two atoms, as shown in Figure 1B. In the FXR crystal structure, the side chain of Arg264 is missing. After completion and MD refinement, the side chain of Arg264 pointed to GW4064 and formed a direct hydrogen bond with the carboxyl group. At the same time, two other hydrogen bonds between GW4064 and Arg331 as well as Met265 found in the crystal structure were maintained during the whole MD process (Figure 1B). The additional hydrogen bonding stabilized the binding of GW4064 in the FXR pocket.

To examine the mobility of the protein residues, the root-mean-square fluctuation (RMSF) of the backbone atoms of FXR during the MD production stage was calculated, as shown in Figure 1C. Aside from the N- and C-terminus, the large fluctuations of residues mainly occur in loops connecting the regular secondary elements. These loops are exposed to the solvent and can readily move. The trend of the calculated RMSF is in general agreement with the deduction from the crystal structures except for the region between H1 and H3 (Supporting Information Figure S2), which exhibited a high mobility during MD simulations. In fact, this region has

considerable flexibility and can adopt different conformations upon different ligands binding.

**Multiple Unbinding Pathways Identified by RAMD Simulations.** RAMD is an effective approach to identify the possible channels of the macromolecules whose active site is deeply buried in the protein core. RAMD has been successfully applied to many systems, including cytochromes P450,<sup>37,45,46</sup> GPCR,<sup>47</sup> NRs,<sup>25,30,31</sup> histone deacetylase,<sup>48</sup> and nicotinic acetylcholine receptor.<sup>49</sup> In this work, we employed this advanced technique to identify the ligand unbinding pathways from FXR. Based on the equilibrated snapshot at 30-ns, 100 RAMD simulations were carried out for each system. The RAMD results were summarized in Table 1. The ligand was

**Table 1. Statistical Summary of RAMD Simulations of GW4064 from FXR**

systems	Path 1			Path 2		Path 3	Path 4
	1A	1B	1C	2A	2B		
FXR/GW4064/AF2	6	6	1	15	28	5	3
FXR/GW4064	2	11	1	7	10	2	4
total	8	17	2	22	38	7	7

found to exit the binding pocket through different pathways. The successful unbinding pathways were clustered together and defined by the secondary structural elements lining them. Four main pathway clusters (Paths 1–4) were found in the FXR complexes, as shown in Figure 2A.

Path 1 has three different ending subdirections, namely 1A, 1B, and 1C. Path 1A is between the H3 middle part and the H11–H12 loop; 1B is located in the opening formed by the H11 C-terminus, H3 N-terminus, H11–H12 loop, and H6–H7 loop; and 1C is between the H2–H3 loop and H6. Path 2 has two different ending orientations. Path 2A is located between the H1–H2 loop and the H5–H6 loop, while Path 2B penetrates through the cleft formed by the H5–H6 loop, H6, and H7. Path 3 is located between H7 and H11, which is close

to Path 1B. Path 4 exists in the area formed by H11, H12, and the H11–H12 loop. Of the four main pathway clusters, the expulsion occurrence frequencies differed remarkably, as shown in Figure 2B. In the FXR/GW4064/AF2 system, the percents of GW4064 unbinding via Paths 1 and 2 are ~20% and ~67%, respectively. The other two pathways Paths 3 and 4 were observed rarely (~8%–~5%).

A recent study by Nilsson's group has mentioned the effect of the bound coactivator peptide on the ligand unbinding pathways.<sup>30</sup> They found that the inclusion of the coactivator peptide had little effect on the ligand unbinding from ERs. In this study, we tried to find out whether the effect exists for FXR. By removing the bound coactivator peptide, the same number of RAMD simulations was performed on the FXR/GW4064 complex. In the FXR/GW4064 system, the unbinding frequencies of Paths 1 and 2 are ~38% and ~46%, respectively. Paths 3 and 4 occupy about ~5% and ~11%, respectively. Comparing the ligand unbinding pathways with and without the coactivator peptide bound, we found that the removal of the coactivator peptide had no impact on the number of the unbinding pathways but had an effect on the pathway distributions. This event is in line with Nilsson's observation in ERs.<sup>30</sup> In the FXR/GW4064 system, Path 2 still has the highest unbinding ratio. The removal of the coactivator peptide did not change the ranking order of Paths 1 and 2 but resulted in an ~18% increase in the unbinding frequencies of Path 1 and an ~21% decrease in that of Path 2.

Path 1A occupies ~8% in all 101 successful unbinding trajectories, but we found that, among all eight successful trajectories, six trajectories had significant helix deformation in the H3 middle part. This renders this pathway unlikely to be the unbinding pathway for the ligand. Path 1C was very rarely observed, only one time for each system. Path 3 leads to the heterodimer surface of FXR with RAR and was also rarely observed in the simulations. This pathway was also ruled out in a similar simulation on VDR.<sup>31</sup> Path 4 is located below H12. Although this pathway was suggested to an entry route

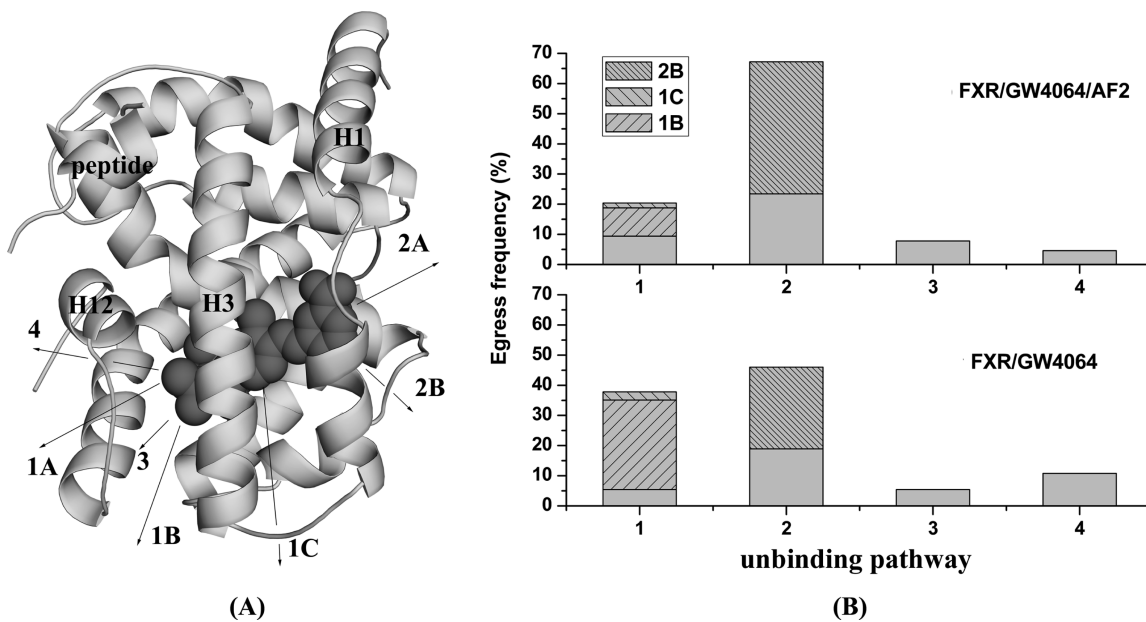


**Figure 2.** (A) GW4064 unbinding pathways from FXR identified by RAMD simulations. The major secondary structural elements of FXR are labeled. GW4064 is represented by black filled sphere. (B) The unbinding frequencies of GW4064 from the FXR/GW4064/AF2 complex (upper panel) and from the FXR/GW4064 complex (lower panel).

according to the mousetrap mechanism, a closed form of the H2 region adopted in the GW4064 bound structures and the rarely occurred unbinding frequency lower the possibility of it as an exit pathway of FXR. Several previous studies on other NRs also did not support this pathway as a favorable unbinding pathway.<sup>23,29–31</sup>

By integrating the numbers of FXR/GW4064 complexes with and without the coactivator peptide bound, it is obvious that three pathways, Paths 1B, 2A, and 2B, have the higher occurrence frequencies for GW4064 unbinding. According to the basic principle of RAMD and many previous RAMD simulations results of other systems, these three pathways are most likely to serve as the unbinding pathway for GW4064. Yet, the preference of these three potential pathways serving as the unbinding pathway of GW4064 warrants further investigation.

The presumed ligand unbinding mechanism in NRs suggested that the ligand would exit from the binding site prior to coactivator dissociation.<sup>30,50</sup> In addition, our RAMD simulations proved that the removal of the coactivator did not significantly change the predominant pathways in FXR. Therefore, the following analysis was only based on the coactivator peptide bound system.

**SMD Simulations.** SMD simulations were conducted for the three most frequently observed unbinding pathways 2A, 2B, and 1B found in RAMD simulations in order to obtain the quantitative estimates of rupture forces. As pointed out by Burendahl et al. in a recent study,<sup>30</sup> compared with RAMD, SMD can sample more extensively for both the ligand and its surrounding residues when pulling along the same pathway as RAMD and thereby allowing a more detailed characterization of the interactions between the ligand and protein residues along a specific unbinding pathway.

**Unbinding along Path 2A.** The representative force profiles of GW4064 unbinding from the binding pocket of FXR along Path 2A are shown in Figure 3A. At the beginning, GW4064

During ~650 ps to ~850 ps, the force maintained a transient stability. At this stage, the dichlorobenzene ring of GW4064 inserted deeper into the space formed by Phe329 and Tyr369 and formed  $\pi-\pi$  interactions with both the residues, as shown in Figure 4A. The isopropyl group of the isoxazole ring had hydrophobic interactions with Ala291, Thr288, and Leu287 of H3. In addition, the middle part of GW4064 formed van der Waals contacts with Ser332 of H5, Met265 of the H1 and H2 loop, and Met290 of H3. Interestingly, although the ligand had a ~4.4 Å movement from its initial position and lost the hydrogen bond with the backbone hydrogen atom of Met265, the strong hydrogen bonding with Arg331 and Arg264 still maintained. Once the hydrogen bond between GW4064 and Arg331 was broken and the dichlorobenzene ring of GW4064 crossed over the blockage of Tyr369, the applied force sharply decreased.

The force peak between ~860 ps and ~1100 ps was attributed to the hydrophobic interactions of the ligand with the residues of H5, H6, and H7 and the hydrogen bonding with Arg264. This hydrogen bond disappeared at ~960 ps, but the strong hydrophobic interactions with Leu348, Ile335, Met265, Met290, Thr370, and Ser332 prevented the ligand from quick releasing (Figure 4A). After the dichlorobenzene ring of GW4064 got rid of the constraints from residues of H6 and H7, GW4064 can exit smoothly. The fluctuations between ~1700 ps and ~2200 ps were due to the interactions of GW4064 with the residues in the FXR surface.

**Unbinding along Path 2B.** Figure 3B depicts the typical force profile of GW4064 unbinding along Path 2B. In the first ~900 ps, the GW4064 unbinding event along Path 2B was similar to that along Path 2A. From ~910 ps to ~1080 ps, the force had a slight increase, which resulted from the face-to-edge  $\pi-\pi$  interactions between the dichlorobenzene ring of GW4064 and the benzene ring of Tyr369 as well as the blockage of the benzene ring of Phe366 in H6. In order for the dichlorobenzene ring of GW4064 to get through the channel, a high force was required to break the hindrance from Phe366 and Tyr369. With the repulsion to Phe366 by the increased applied force, the benzene ring of Phe366 was forced to rotate, which led to an expansion of the pathway (Figure 4B). As such, the hindrance from Phe366 disappeared, which was displayed by a significant decrease in the applied force at ~1120 ps. At this point, the carboxyl group of GW4064 kept almost at the initial position and maintained the direct hydrogen bonds with the guanidine side chain of Arg331, NH1 of Arg264, and the backbone amine hydrogen of Met265.

During ~1120 ps to ~1440 ps, the hydrogen bonds between GW4064 and Arg331, Arg264, and Met265 were broken in succession. However, the strong hydrophobic interactions of GW4064 with Phe366, Tyr369, Ile352, Leu348, Leu340, and Ile335 made up the loss of hydrogen bonding interactions. This was reflected by a relatively small fluctuation in the force profile during this period. The force peak formed at ~1500 ps was contributed to the hydrogen bond formed between Ser332 and GW4064 (Figure 4B).

**Unbinding along Path 1B.** Figure 3C shows the typical force profile of GW4064 unbinding through Path 1B. The applied force had a remarkable decrease at ~650 ps, which was mainly caused by the loss of the hydrogen bonds of the ligand with Arg264 and His447. The hydrogen bonds of GW4064 with Arg331 and Met265 were lost at ~650 ps, but with the movement, the benzoic carboxyl group of GW4064 was close to His325 and formed a direct hydrogen bond with it (Figure

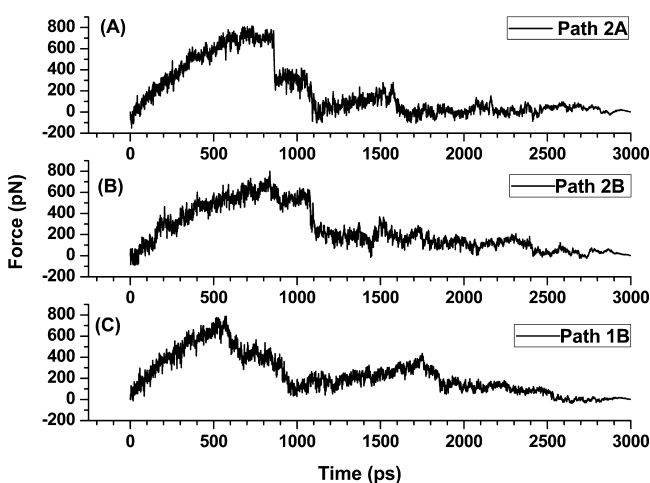


**Figure 3.** The typical force profiles of pulling GW4064 out of the FXR pocket along Path 2A (A), Path 2B (B), and Path 1B (C), respectively.

was held tightly in the binding pocket by the strong hydrogen bonding with His447, Arg264, and Arg331 and the hydrophobic interactions with Met265, Thr288, Ala291, Phe329, Ile335, and Trp454. After ~600 ps, the hydrogen bond between His447 and GW4064 was broken and thus weakening the interactions of the ligand with FXR.

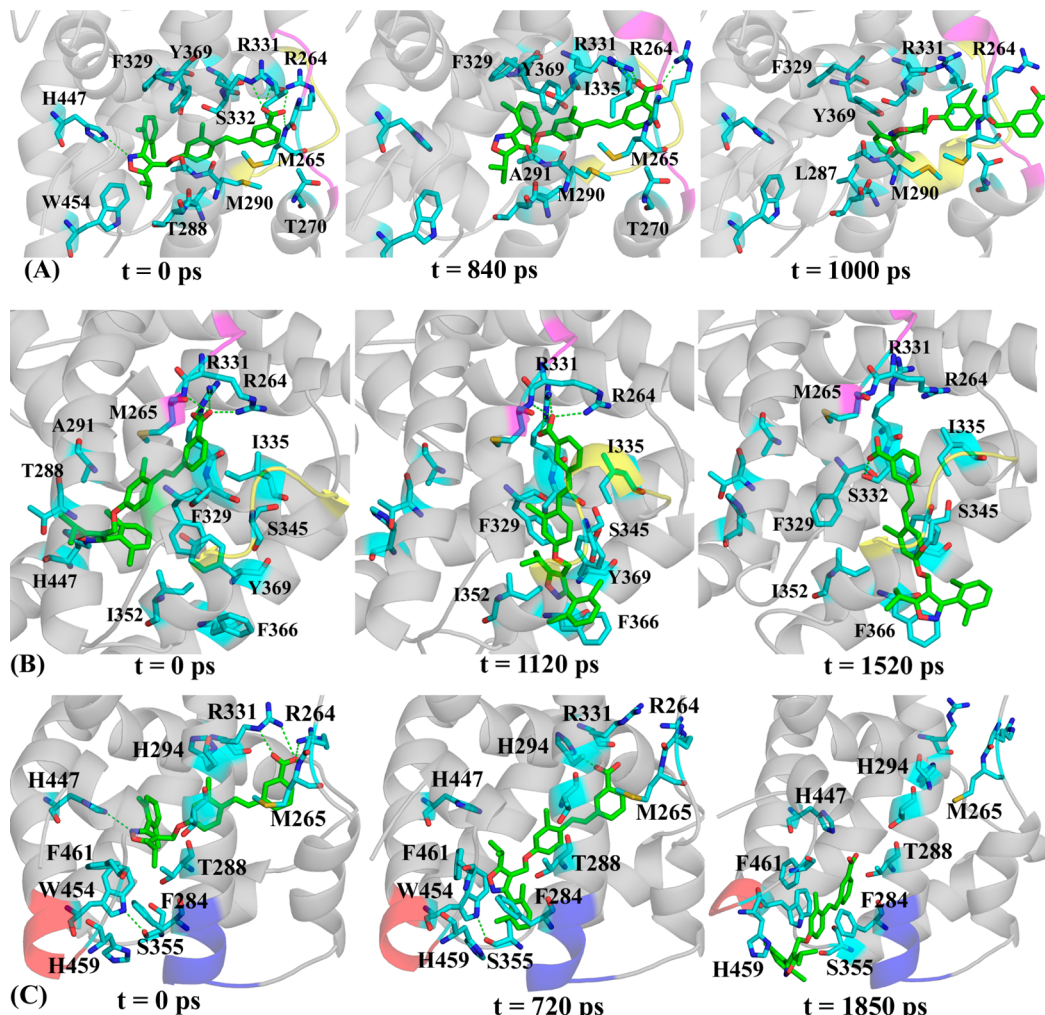


**Figure 4.** Snapshots of GW4064 unbinding from FXR along Path 2A (A), Path 2B (B), and Path 1B (C). Important residues interacting with the ligand are labeled and shown as sticks. The hydrogen bonds are shown in green dotted lines. The H1–H2 loop is shown in magentas, the H5–H6 loop in yellow, the H3 N-terminus in blue, and the H11 C-terminus in red.

4C). At this stage, the ligand formed  $\pi$ - $\pi$  interactions with Trp454 of H11 first via its dichlorobenzene ring and then via the isoxazole ring. At the same time, the isopropyl group in the isoxazole ring pointed to the phenyl side chains of Phe284 of H3 and Phe461 of the H11–H12 loop.

The side chains of Phe284 in H3 and His459 in the H11–H12 loop reside at the two sides of the Path 1B entrance and thus blocking the leaving of GW4064. Subsequently, the side chains of these two residues underwent a rotation to expand the opening of Path 1B. Once the ligand crossed over the blockage from these two residues, the applied force decreased to a local minimum. From ~990 ps to ~1890 ps, the fluctuation of the applied force was attributed to the van der Waals contacts of GW4064 with the residues in H3, H11, H6, and the H11–H12 loop, which include Leu287, Phe284, Ile352, Phe461, Trp454, and His459 (Figure 4C). The slight decrease in the force at ~1880 ps was because of the breakage of the hydrogen bond formed between the carboxyl group of GW4064 and His447.

**Comparative Analysis of GW4064 Unbinding along Three Pathways.** The maximum force value ( $F_{max}$ ) and the sum of the force ( $F_{sum}$ ) were extracted from the individual SMD simulation trajectories (Supporting Information Figure S3 and Table S2). It is worth noting that the free energy of unbinding should be calculated in order to obtain a precise, reliable

estimate about the relative preference of the ligand unbinding pathways. Although the free energy of unbinding can be estimated from the nonequilibrium SMD simulations by using Jarzynski's equality,<sup>51</sup> enough samplings with a very low velocity are required to obtain a converged free energy. This makes the simulations relatively expensive and is not attainable in practice. In addition, according to our own experiences<sup>37,45</sup> and the results from several other groups,<sup>49,52,53</sup> the potential of mean force estimates based on Jarzynski's equality by using approximation methods often resulted in a large deviation from the real free energy. Therefore, the expensive sampling simulations were not carried out in this study. Instead, the maximum force value and the sum of the force were used to estimate the pathway preference, which has been widely used in many previous studies on other NRs.<sup>27,30,31</sup>

The average values of  $F_{max}$  and  $F_{sum}$  from ten SMD trajectories are presented in Table 2. Because the  $F_{sum}$  value is heavily dependent on the saved data points, an arbitrary unit is given to avoid misleading of it as a real energy, which was also adopted by a recent study.<sup>30</sup> Based on the calculated values of  $F_{max}$  and  $F_{sum}$  no consistent conclusion can be drawn. However, neither  $F_{max}$  nor  $F_{sum}$  supports Path 1B as a favorable GW4064 unbinding pathway.

**Table 2.** Average Values of  $F_{max}$  and  $F_{sum}$  along Three Distinct Pathways

pathways	$F_{max}$ (pN)	$F_{sum}$
Path 2A	$799 \pm 16^a$	$658,725 \pm 30,127$
Path 2B	$661 \pm 20$	$665,406 \pm 13,550$
Path 1B	$743 \pm 13$	$758,037 \pm 28,244$

<sup>a</sup>The uncertainties are the standard error of the mean calculated with 10 SMD simulations.

We also analyzed the movement of the  $C\alpha$  atoms of those residues lining the pathway. Superposition of the SMD trajectory with the starting structure revealed that unbinding of GW4064 along Path 2A required a bending of the H1–H2 loop as well as the H5–H6 loop. The  $C\alpha$  displacements were observed for several residues in these two loops to facilitate the escape of GW4064. The maximum  $C\alpha$  displacement was found  $\sim 4.7$  Å for Glu268 in the H1–H2 loop and  $\sim 4.0$  Å for Pro341 in the H5–H6 loop. Unbinding of GW4064 along Path 2B required  $\sim 4.9$  Å and  $\sim 4.6$  Å shift outward for the  $C\alpha$  atoms of Phe336 and Asn337 in the H5 N-terminus, respectively, and  $\sim 4.1$  Å shift for the  $C\alpha$  atom of Asp346 in the H6 C-terminus. Unbinding of GW4064 along Path 1B required  $\sim 6.0$  Å shift in the H3 N-terminus and  $\sim 9.0$  Å shift in the H11 N-terminus. In addition, for GW4064 to escape along this pathway, the hydrogen bond between Trp454 in H11 and Ser355 in the H6–H7 loop needs to be broken to make room for the entrance of Path 1B. The larger structural changes occurred for Path 1B also reduce the possibility of it as a pathway for GW4064 unbinding from FXR. In light of the RAMD results and the force extracted from SMD simulations, both Paths 2A and 2B are considered to be the likely unbinding pathway for GW4064.

**Further Evidence of Path 2A and 2B as the Ligand Unbinding Pathways.** Path 2A serving as a ligand unbinding pathway has been reported by several previous studies. Mikael Peräkylä<sup>31</sup> reported that Path 2A was a predominant and the most favorable pathway for vitamin D unbinding from its

receptor. This pathway is also a favorable pathway for the ligand unbinding in ERs.<sup>30</sup> Interestingly, the crystal structure of FXR complexed with a benzimidazole derivative (PDB code: 3OKH)<sup>54</sup> reveals that two ligands coexist in the FXR pocket. One ligand is normally bound in the hydrophobic pocket as other ligands, while the other is located between the H1–H2 loop and the H5–H6 loop, where is the exit of Path 2A. This unique structure may be considered as the crystallographic evidence that Path 2A can serve as a ligand unbinding pathway. Path 2B has been observed in several NRs, such as VDR, RAR, and ERs. Although this pathway showed a low possibility as an unbinding pathway in these NRs, our results indicate that Path 2B as a pathway for GW4064 unbinding from FXR cannot be ruled out. In fact, multiple ligand unbinding pathways have been observed in several NRs<sup>25,30,31</sup> and other systems.<sup>37,45–49</sup>

**Gating Mechanisms of Path 2A and 2B.** By analyzing the trajectories of GW4064 unbinding along Path 2A and 2B, we found that some gating residues played important roles in the ligand unbinding. In Path 2A, Tyr369 acted as a gatekeeper to block the ligand leaving the binding pocket. The phenol side chain of Tyr369 points to the inside of the binding pocket and occupies part of the pathway space. The appropriate swing and rotation of the phenol side chain are needed to expand the space in order to allow GW4064 unbinding. To qualify the rotation, the variation of the side chain torsion  $\chi$  (CA, CB, CG, and CD2) of Tyr369 was measured during the SMD simulation, as shown in Figure 5A and 5B. The torsion angle has a significant change from 600 to 1100 ps. The swing of the Tyr369 side chain forced the benzene ring of Phe336 to undergo a displacement. Tyr369 has been found to be an important residue to stabilize the ligand binding in the FXR pocket. The crystal structures of FXR with benzimidazole derivatives<sup>54</sup> (PDB codes: 3OKH, 3OKI, 3OMK, and 3OOK) show that Tyr369 forms a direct hydrogen bond with one of the nitrogen atoms of the ligands. The crystal structures of FXR with CDCA<sup>55</sup> as well as with XL335 derivatives<sup>56</sup> confirm such direct hydrogen bonds are formed between Tyr369 and the ligand. Although no such a direct hydrogen bond is found in

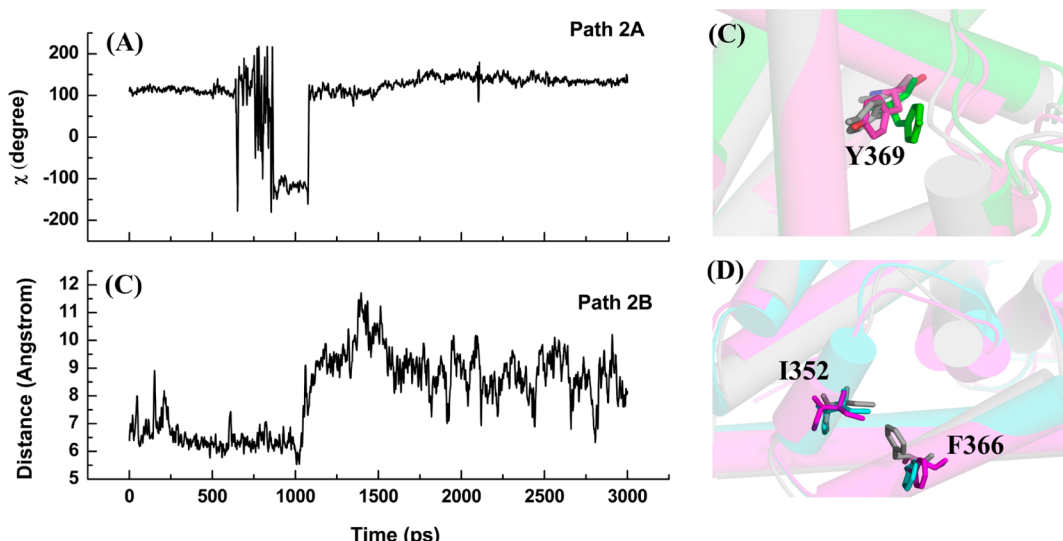


**Figure 5.** The variation of the side chain torsion  $\chi$  (CA, CB, CG, and CD2) of Tyr369 with respect to simulation time during GW4064 unbinding along Path 2A. (B) The orientations of Tyr369 at 0 ps (gray), 840 ps (green), and 2000 ps (magenta) when unbinding via Path 2A. (C) The variation of the distance between Phe366 and Ile352 versus simulation time. (D) The orientations of Phe366 and Ile352 at 0 ps (gray), 1440 ps (magenta), and 2000 ps (cyan) when unbinding via Path 2B.

FXR-GW4064 complex, Tyr369 has a role in preventing GW4064 from escaping the binding pocket and thus maintaining its activity.

In Path 2B, in addition to a similar event occurred for Tyr369, the benzene ring of Phe366 had a wiggle, which is manifested by the variation of the distance between Phe366 and Ile352 (Figure 5C and 5D). Both residues are located at the entrance of Path 2B. The distance becomes wider from  $\sim$ 1100 ps to facilitate passage of the dichlorobenzene ring of GW4064.

Although Paths 2A and 2B share some common residues lining the individual pathway, the dissociation manners of GW4064 along these two pathways differed significantly. The dissociation of GW4064 along Path 2A is parallel to its binding orientation in the FXR binding pocket, as shown in Figure 6.

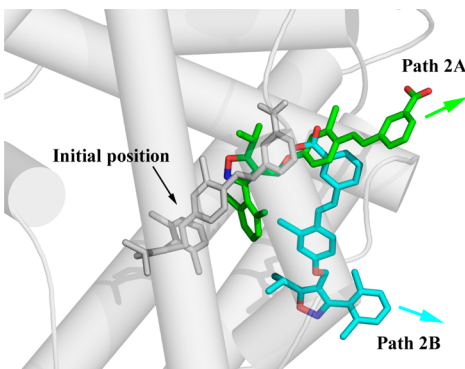


**Figure 6.** The different unbinding manners of GW4064 from FXR along Path 2A (green) and Path 2B (cyan).

The hydrogen bond between GW4064 and His447 disrupted first (Supporting Information Figure S4), and then with the movement of GW4064, the guanidine side chains of Arg331 and Arg264 were accompanied to move. After that, the salt bridge of GW4064 with Arg331 was broken, followed by the breakage of the hydrogen bond of GW4064 with Arg264. The dichlorobenzene ring was finally passing through the exit of Path 2A. While the unbinding of GW4064 along Path 2B also started with the breakage of the hydrogen bond with His447, the dichlorobenzene ring moved first in a direction perpendicular to Path 2A. Before the dichlorobenzene ring moved out of the exit of Path 2B, the hydrogen bonds between GW4064 and the guanidine side chains of Arg331 and Arg264 were maintained. Only if the isoxazole ring and the dichlorobenzene ring were completely exposed to the solvent, the hydrogen bonds of GW4064 with Arg331 and Arg264 then started to break. In a word, the benzoic acid moiety of GW4064 first moved out the exit along Path 2A, while the dichlorobenzene ring moiety of GW4064 first moved along Path 2B (Figure 6).

**Implications for the Structural Modification of GW4064.** Based on the interactions between GW4064 and the residues lining the unbinding pathways, several structural determinants may be essential to maintain its activity. First, the hydrogen bonds formed between the carboxyl group of the ligand and Arg331 and Arg264 are crucial not only for stabilizing the ligand binding but also for preventing its escape. These interactions are definitely important for maintaining the activity of GW4064. Within the appropriate distance and angles, the carboxyl group might be replaced by other groups with negative charges or electron donors, such as sulfate and amide groups. Second, the dichlorobenzene ring is another

important group for GW4064. During the unbinding process, this group inserted the hydrophobic space between Tyr369 and Phe329 and formed  $\pi-\pi$  interactions with Try369. Therefore, a substitution at ortho- and meta-position of the benzene ring by a small, hydrophobic group such as a methyl group would be allowed, but destruction of the conjugate  $\pi$  electron cloud should be avoided. Third, because the middle part of GW4064 mainly formed hydrophobic interactions with its surrounding residues, a slight modification at this region by hydrophobic groups such as fluoro- and methylbenzene would be tolerated.

## CONCLUSIONS

Due to the important roles of NRs in drug discovery for many metabolic diseases, the unbinding pathways and associated unbinding mechanisms of these receptors have attracted much attention in recent years. A recent study<sup>19,20</sup> that successfully designed new enzyme inhibitors based on the unbinding pathways aroused our interest in exploring the FXR-GW4064 complex systems. Our results support the coexistence of multiple unbinding pathways that has been seen in other NRs and other systems. Two pathways are determined for GW4064 unbinding from FXR: one is between the H1–H2 loop and the H5–H6 loop, and the other is through the cleft formed by the H5–H6 loop, H6, and H7. Analysis of the RAMD and SMD trajectories reveals that the unbinding manners of GW4064 differed from each other in these two pathways. The possible strategies of designing new GW4064 derivatives were also proposed based on the findings. These results will provide insights into the action mechanism of GW4064 with FXR and be helpful for rational design of new FXR ligands.

## ASSOCIATED CONTENT

### Supporting Information

Supplemental figures (Figures S1 to S4) and tables (Tables S1 and S2). This material is available free of charge via the Internet at <http://pubs.acs.org>.

## AUTHOR INFORMATION

### Corresponding Author

\*Phone: +86-21-6425-1052. Fax: +86-21-6425-1033. E-mail: myzheng@mail.shcnc.ac.cn (M.Z.), ytang234@ecust.edu.cn (Y.T.).

### Notes

The authors declare no competing financial interest.

## ACKNOWLEDGMENTS

This work was supported by the State Key Laboratory of Drug Research (SIMM1106KF-07), the National Natural Science Foundation of China (Grant 21072059), the Shanghai Committee of Science and Technology (Grant 11DZ2260600), and the Scientific Research Foundation for the Returned Overseas Chinese Scholars, Ministry of Education of China.

## REFERENCES

- (1) Lopez-Velazquez, J. A.; Castro-Torres, I. G.; Sanchez-Valle, V.; Mendez-Sanchez, N. Intestinal nuclear bile acid receptor FXR and cholestasis. *Ann. Hepatol.* **2012**, *11*, 152–154.
- (2) Fiorucci, S.; Mencarelli, A.; Distrutti, E.; Zampella, A. Farnesoid X receptor: from medicinal chemistry to clinical applications. *Future Med. Chem.* **2012**, *4*, 877–891.
- (3) Cariou, B.; Staels, B. FXR: a promising target for the metabolic syndrome? *Trends Pharmacol. Sci.* **2007**, *28*, 236–243.

- (4) Lee, F. Y.; Lee, H.; Hubbert, M. L.; Edwards, P. A.; Zhang, Y. FXR, a multipurpose nuclear receptor. *Trends Biochem. Sci.* **2006**, *31*, 572–580.
- (5) Evans, M. J.; Mahaney, P. E.; Borges-Marcucci, L.; Lai, K.; Wang, S.; Krueger, J. A.; Gardell, S. J.; Huard, C.; Martinez, R.; Vlasuk, G. P.; Harnish, D. C. A synthetic farnesoid X receptor (FXR) agonist promotes cholesterol lowering in models of dyslipidemia. *Am. J. Physiol.: Gastrointest. Liver Physiol.* **2009**, *296*, G543–G552.
- (6) Zhang, Y.; Lee, F. Y.; Barrera, G.; Lee, H.; Vales, C.; Gonzalez, F. J.; Willson, T. M.; Edwards, P. A. Activation of the nuclear receptor FXR improves hyperglycemia and hyperlipidemia in diabetic mice. *Proc. Natl. Acad. Sci. U.S.A.* **2006**, *103*, 1006–1011.
- (7) Pellicciari, R.; Costantino, G.; Fiorucci, S. Farnesoid X receptor: from structure to potential clinical applications. *J. Med. Chem.* **2005**, *48*, 5383–5403.
- (8) Wang, Y. D.; Chen, W. D.; Huang, W. FXR, a target for different diseases. *Histol. Histopathol.* **2008**, *23*, 621–627.
- (9) Crawley, M. L. Farnesoid X receptor modulators: a patent review. *Expert Opin. Ther. Pat.* **2010**, *20*, 1047–1057.
- (10) Merk, D.; Steinhilber, D.; Schubert-Zsilavecz, M. Medicinal chemistry of farnesoid X receptor ligands: from agonists and antagonists to modulators. *Future Med. Chem.* **2012**, *4*, 1015–1036.
- (11) Cyphert, H. A.; Ge, X.; Kohan, A. B.; Salati, L. M.; Zhang, Y.; Hillgartner, F. B. Activation of the farnesoid x receptor induces hepatic expression and secretion of fibroblast growth factor 21. *J. Biol. Chem.* **2012**, *287*, 25123–25138.
- (12) Xu, Z.; Huang, G.; Gong, W.; Zhou, P.; Zhao, Y.; Zhang, Y.; Zeng, Y.; Gao, M.; Pan, Z.; He, F. FXR ligands protect against hepatocellular inflammation via SOCS3 induction. *Cell Signalling* **2012**, *24*, 1658–1664.
- (13) Gadaleta, R. M.; Oldenburg, B.; Willemsen, E. C.; Spit, M.; Murzilli, S.; Salvatore, L.; Klompm, L. W.; Siersema, P. D.; van Erpecum, K. J.; van Mil, S. W. Activation of bile salt nuclear receptor FXR is repressed by pro-inflammatory cytokines activating NF-kappaB signaling in the intestine. *Biochim. Biophys. Acta* **2011**, *1812*, 851–858.
- (14) Renga, B.; Migliorati, M.; Mencarelli, A.; Cipriani, S.; D’Amore, C.; Distrutti, E.; Fiorucci, S. Farnesoid X receptor suppresses constitutive androstane receptor activity at the multidrug resistance protein-4 promoter. *Biochim. Biophys. Acta* **2011**, *1809*, 157–165.
- (15) Akwabi-Ameyaw, A.; Bass, J. Y.; Caldwell, R. D.; Caravella, J. A.; Chen, L.; Creech, K. L.; Deaton, D. N.; Madauss, K. P.; Marr, H. B.; McFadyen, R. B.; Miller, A. B.; Navas, F., III; Parks, D. J.; Spearing, P. K.; Todd, D.; Williams, S. P.; Bruce Wisely, G. FXR agonist activity of conformationally constrained analogs of GW 4064. *Bioorg. Med. Chem. Lett.* **2009**, *19*, 4733–4739.
- (16) Akwabi-Ameyaw, A.; Bass, J. Y.; Caldwell, R. D.; Caravella, J. A.; Chen, L.; Creech, K. L.; Deaton, D. N.; Jones, S. A.; Kaldor, I.; Liu, Y.; Madauss, K. P.; Marr, H. B.; McFadyen, R. B.; Miller, A. B.; Iii, F. N.; Parks, D. J.; Spearing, P. K.; Todd, D.; Williams, S. P.; Wisely, G. B. Conformationally constrained farnesoid X receptor (FXR) agonists: naphthoic acid-based analogs of GW 4064. *Bioorg. Med. Chem. Lett.* **2008**, *18*, 4339–4343.
- (17) Bass, J. Y.; Caravella, J. A.; Chen, L.; Creech, K. L.; Deaton, D. N.; Madauss, K. P.; Marr, H. B.; McFadyen, R. B.; Miller, A. B.; Mills, W. Y.; Navas, F., III; Parks, D. J.; Smalley, T. L., Jr.; Spearing, P. K.; Todd, D.; Williams, S. P.; Wisely, G. B. Conformationally constrained farnesoid X receptor (FXR) agonists: heteroaryl replacements of the naphthalene. *Bioorg. Med. Chem. Lett.* **2011**, *21*, 1206–1213.
- (18) Akwabi-Ameyaw, A.; Caravella, J. A.; Chen, L.; Creech, K. L.; Deaton, D. N.; Madauss, K. P.; Marr, H. B.; Miller, A. B.; Navas, F., III; Parks, D. J.; Spearing, P. K.; Todd, D.; Williams, S. P.; Wisely, G. B. Conformationally constrained farnesoid X receptor (FXR) agonists: alternative replacements of the stilbene. *Bioorg. Med. Chem. Lett.* **2011**, *21*, 6154–6160.
- (19) Colizzi, F.; Perozzo, R.; Scapozza, L.; Recanatini, M.; Cavalli, A. Single-molecule pulling simulations can discern active from inactive enzyme inhibitors. *J. Am. Chem. Soc.* **2010**, *132*, 7361–7371.
- (20) Jorgensen, W. L. Drug discovery: pulled from a protein’s embrace. *Nature* **2010**, *466*, 42–43.
- (21) Huang, P.; Chandra, V.; Rastinejad, F. Structural overview of the nuclear receptor superfamily: insights into physiology and therapeutics. *Annu. Rev. Physiol.* **2010**, *72*, 247–272.
- (22) Renaud, J. P.; Rochel, N.; Ruff, M.; Vivat, V.; Chambon, P.; Gronemeyer, H.; Moras, D. Crystal structure of the RAR-gamma ligand-binding domain bound to all-trans retinoic acid. *Nature* **1995**, *378*, 681–689.
- (23) Kosztin, D.; Izrailev, S.; Schulten, K. Unbinding of retinoic acid from its receptor studied by steered molecular dynamics. *Biophys. J.* **1999**, *76*, 188–197.
- (24) Blondel, A.; Renaud, J. P.; Fischer, S.; Moras, D.; Karplus, M. Retinoic acid receptor: a simulation analysis of retinoic acid binding and the resulting conformational changes. *J. Mol. Biol.* **1999**, *291*, 101–115.
- (25) Carlsson, P.; Burendahl, S.; Nilsson, L. Unbinding of retinoic acid from the retinoic acid receptor by random expulsion molecular dynamics. *Biophys. J.* **2006**, *91*, 3151–3161.
- (26) Martinez, L.; Sonoda, M. T.; Webb, P.; Baxter, J. D.; Skaf, M. S.; Polikarpov, I. Molecular dynamics simulations reveal multiple pathways of ligand dissociation from thyroid hormone receptors. *Biophys. J.* **2005**, *89*, 2011–2023.
- (27) Martinez, L.; Webb, P.; Polikarpov, I.; Skaf, M. S. Molecular dynamics simulations of ligand dissociation from thyroid hormone receptors: evidence of the likeliest escape pathway and its implications for the design of novel ligands. *J. Med. Chem.* **2006**, *49*, 23–26.
- (28) Sonoda, M. T.; Martinez, L.; Webb, P.; Skaf, M. S.; Polikarpov, I. Ligand dissociation from estrogen receptor is mediated by receptor dimerization: evidence from molecular dynamics simulations. *Mol. Endocrinol.* **2008**, *22*, 1565–1578.
- (29) Shen, J.; Li, W.; Liu, G.; Tang, Y.; Jiang, H. Computational insights into the mechanism of ligand unbinding and selectivity of estrogen receptors. *J. Phys. Chem. B* **2009**, *113*, 10436–10444.
- (30) Burendahl, S.; Danciulessu, C.; Nilsson, L. Ligand unbinding from the estrogen receptor: a computational study of pathways and ligand specificity. *Proteins* **2009**, *77*, 842–856.
- (31) Perakyla, M. Ligand unbinding pathways from the vitamin D receptor studied by molecular dynamics simulations. *Eur. Biophys. J.* **2009**, *38*, 185–198.
- (32) Genest, D.; Garnier, N.; Arrault, A.; Marot, C.; Morin-Allory, L.; Genest, M. Ligand-escape pathways from the ligand-binding domain of PPARgamma receptor as probed by molecular dynamics simulations. *Eur. Biophys. J.* **2008**, *37*, 369–379.
- (33) Li, H.; Robertson, A. D.; Jensen, J. H. Very fast empirical prediction and interpretation of protein pKa values. *Proteins* **2005**, *61*, 704–721.
- (34) Gilson, M. K.; Sharp, K. A.; Honig, B. H. Calculating the electrostatic potential of molecules in solution. *J. Comput. Chem.* **1988**, *9*, 327–335.
- (35) Case, D. A.; Cheatham, T. E., III; Darden, T.; Gohlke, H.; Luo, R.; Merz, K. M., Jr.; Onufriev, A.; Simmerling, C.; Wang, B.; Woods, R. J. The Amber biomolecular simulation programs. *J. Comput. Chem.* **2005**, *26*, 1668–1688.
- (36) Jorgensen, W. L.; Chandrasekhar, J.; Madura, J.; Klein, M. L. Comparison of simple potential functions for simulating liquid water. *J. Chem. Phys.* **1983**, *79*, 926–935.
- (37) Li, W.; Shen, J.; Liu, G.; Tang, Y.; Hoshino, T. Exploring coumarin egress channels in human cytochrome P450 2A6 by random acceleration and steered molecular dynamics simulations. *Proteins* **2011**, *79*, 271–281.
- (38) Li, W.; Ode, H.; Hoshino, T.; Liu, H.; Tang, Y.; Jiang, H. Reduced catalytic activity of P450 2A6 mutants with coumarin: A computational investigation. *J. Chem. Theory Comput.* **2009**, *5*, 1411–1420.
- (39) Ryckaert, J. P.; Ciccotti, G.; Berendsen, H. J. C. Numerical integration of the cartesian equations of motion of a system with constraints: molecular dynamics of n-alkanes. *J. Comput. Phys.* **1977**, *23*, 327–341.

- (40) Essmann, U.; Perera, L.; Berkowitz, W. L.; Darden, T.; Lee, H.; Pedersen, L. G. A smooth particle mesh ewald potential. *J. Chem. Phys.* **1995**, *103*, 8577–8592.
- (41) Schleinkofer, K.; Sudarko; Winn, P. J.; Ludemann, S. K.; Wade, R. C. Do mammalian cytochrome P450s show multiple ligand access pathways and ligand channelling? *EMBO Rep.* **2005**, *6*, 584–589.
- (42) Ludemann, S. K.; Lounnas, V.; Wade, R. C. How do substrates enter and products exit the buried active site of cytochrome P450cam? 1. Random expulsion molecular dynamics investigation of ligand access channels and mechanisms. *J. Mol. Biol.* **2000**, *303*, 797–811.
- (43) Grubmuller, H.; Heymann, B.; Tavan, P. Ligand binding: molecular mechanics calculation of the streptavidin-biotin rupture force. *Science* **1996**, *271*, 997–999.
- (44) Isralewitz, B.; Gao, M.; Schulten, K. Steered molecular dynamics and mechanical functions of proteins. *Curr. Opin. Struct. Biol.* **2001**, *11*, 224–230.
- (45) Shen, Z.; Cheng, F.; Xu, Y.; Fu, J.; Xiao, W.; Shen, J.; Liu, G.; Li, W.; Tang, Y. Investigation of indazole unbinding pathways in CYP2E1 by molecular dynamics simulations. *PLoS One* **2012**, *7*, e33500.
- (46) Cojocaru, V.; Winn, P. J.; Wade, R. C. Multiple, ligand-dependent routes from the active site of cytochrome P450 2C9. *Curr. Drug Metab.* **2012**, *13*, 143–154.
- (47) Wang, T.; Duan, Y. Chromophore channeling in the G-protein coupled receptor rhodopsin. *J. Am. Chem. Soc.* **2007**, *129*, 6970–6971.
- (48) Kalyaanamoorthy, S.; Chen, Y. P. Exploring inhibitor release pathways in histone deacetylases using random acceleration molecular dynamics simulations. *J. Chem. Inf. Model.* **2012**, *52*, 589–603.
- (49) Yu, R.; Kaas, Q.; Craik, D. J. Delineation of the unbinding pathway of alpha-conotoxin ImI from the alpha7 nicotinic acetylcholine receptor. *J. Phys. Chem. B* **2012**, *116*, 6097–6105.
- (50) Tsai, M. J.; O’Malley, B. W. Molecular mechanisms of action of steroid/thyroid receptor superfamily members. *Annu. Rev. Biochem.* **1994**, *63*, 451–486.
- (51) Jarzynski, C. Nonequilibrium equality for free energy differences. *Phys. Rev. Lett.* **1997**, *78*, 2690–2693.
- (52) Grater, F.; de Groot, B. L.; Jiang, H.; Grubmuller, H. Ligand-release pathways in the pheromone-binding protein of *Bombyx mori*. *Structure* **2006**, *14*, 1567–1576.
- (53) Cuendet, M. A.; Michelin, O. Protein-protein interaction investigated by steered molecular dynamics: the TCR-pMHC complex. *Biophys. J.* **2008**, *95*, 3575–3590.
- (54) Richter, H. G.; Benson, G. M.; Bleicher, K. H.; Blum, D.; Chaput, E.; Cleemann, N.; Feng, S.; Gardes, C.; Grether, U.; Hartman, P.; Kuhn, B.; Martin, R. E.; Plancher, J. M.; Rudolph, M. G.; Schuler, F.; Taylor, S. Optimization of a novel class of benzimidazole-based farnesoid X receptor (FXR) agonists to improve physicochemical and ADME properties. *Bioorg. Med. Chem. Lett.* **2011**, *21*, 1134–1140.
- (55) Mi, L. Z.; Devarakonda, S.; Harp, J. M.; Han, Q.; Pellicciari, R.; Willson, T. M.; Khorasanizadeh, S.; Rastinejad, F. Structural basis for bile acid binding and activation of the nuclear receptor FXR. *Mol. Cell* **2003**, *11*, 1093–1100.
- (56) Flatt, B.; Martin, R.; Wang, T. L.; Mahaney, P.; Murphy, B.; Gu, X. H.; Foster, P.; Li, J.; Pircher, P.; Petrowski, M.; Schulman, I.; Westin, S.; Wrobel, J.; Yan, G.; Bischoff, E.; Daige, C.; Mohan, R. Discovery of XL335 (WAY-362450), a highly potent, selective, and orally active agonist of the farnesoid X receptor (FXR). *J. Med. Chem.* **2009**, *52*, 904–907.